The Astrophysical Journal, 892:129 (14pp), 2020 April 1 https://doi.org/10.3847/1538-4357/ab799a

Formation of Post-CME Blobs Observed by LASCO-C2 and K-Cor on 2017 September 10

Jae-Ok Lee[1], Kyung-Suk Cho[1,2], Kyoung-Sun Lee[3], Il-Hyun Cho[4], Junggi Lee[5], Yukinaga Miyashita[1], Yeon-Han Kim[1], Rok-Soon Kim[1], and Soojeong Jang[1]
[1] Space Science Division, Korea Astronomy and Space Science Institute, Daejeon 34055, Republic of Korea
[2] Department of Astronomy and Space Science, University of Science and Technology, Daejeon 34055, Republic of Korea
[3] Center for Space Plasma and Aeronomic Research, University of Alabama in Huntsville, Huntsville, AL 35805, USA
[4] Department of Astronomy and Space Science, Kyung Hee University, Yongin 17104, Republic of Korea
[5] School of Space Research, Kyung Hee University, Yongin 17104, Republic of Korea
Received 2020 January 9; revised 2020 February 17; accepted 2020 February 19; published 2020 April 6

Abstract

Understanding the formation of post-CME blobs, we investigate 2 blobs in the outer corona observed by LASCO-C2 and 34 blobs in the inner corona by K-Cor on 2017 September 10 from 17:11 to 18:58 UT. By visual inspection of the structure of a post-CME current sheet (CS) and its associated blobs, we find that the CS is well identified in the K-Cor and its radial lengths are nine times longer than lateral widths, indicating the CS is unstable to the linear tearing mode. The inner corona blobs can be classified into two groups: 27 blobs generated in the middle of the CS (Group 1) and 7 blobs occurred above the tips of it (Group 2). Their lateral widths are $\langle 0.02R_{\odot}\rangle$ and $\langle 0.05R_{\odot}\rangle$, which is smaller than, or similar to, those ($\langle 0.06R_{\odot}\rangle$) of the CS. They have elongated shapes: ratios of lateral to radial widths are $\langle 0.53\rangle$ and $\langle 0.40\rangle$, respectively. In the first group, only three blobs propagate above the tip of the CS while the others are located in the CS. In the second group, only two blobs have associations with those of outer corona in their temporal and spatial relationship and their initial heights are 1.81 and 1.95 $R_{\odot}$, measured from the center of the Sun. The others cannot be identified in the outer corona. Our results first demonstrate that LASCO-C2 blobs could be generated by the tearing mode instability near the tips of post-CME CSs, similar to the magnetic reconnection process in the tail CS of Earth's magnetosphere.

Unified Astronomy Thesaurus concepts: Solar magnetic reconnection (1504); Solar corona (1483); Solar coronal mass ejections (310)

1. Introduction

A coronal mass ejection (CME) is an explosive phenomenon that occurs in the solar corona. It expels massive amounts of coronal material and magnetic fields into interplanetary space. After the CME erupts, a new narrow bright coronal ray structure develops in the wake of the CME. Occasionally, localized brightness enhancement structures (plasma blobs) along the new narrow bright coronal ray move outward (anti-sunward). These kinds of coronal ray structure and plasma blobs are called post-CME ray and post-CME blobs, which are frequently observed in the space-based white light coronagraphs such as the Large Angle Spectroscopic COronagraph (LASCO; Brueckner et al. 1995) C2 and C3 on board the *Solar and Heliospheric Observatory* (*SOHO*) spacecraft and Sun Earth Connection Coronal and Heliospheric Investigation (SECCHI; Howard et al. 2008) COR-2 on board the *Solar TErrestrial Relations Observatory* (*STEREO*) spacecraft as well as the ground-based white light coronagraph such as the MK-4 coronameter and COronal Solar Magnetism Observatory (COSMO) K-coronagraph (K-Cor) on the Mauna Loa Solar Observatory. Several researchers investigate the post-CME rays and their associated blobs with the coronagraphs and/or Extreme Ultra Violet (EUV) telescopes (Ko et al. 2003; Webb et al. 2003; Lin et al. 2005; Ling & Webb et al. 2014; Lin et al. 2015; Cheng et al. 2018). They have interpreted the post-CME rays as post-CME current sheets (CSs) because their observational structures —post-CME rays seem to connect post-flare loops (or arcade) with the trailing edge of the CME flux rope—are similar to those from the erupting CME flux rope model developed by Lin & Forbes (2000). They also regard the post-CME blobs as a consequence of the magnetic reconnection process inside the CSs.

Theoretically, post-CME blobs can move sunward or outward depending on their formation heights relative to the magnetic reconnection regions including magnetic X-points located in the post-CME CS (Lin & Forbes 2000; Shen et al. 2011; Mei et al. 2012; Forbes et al. 2018). However, many observational studies using LASCO-C2 (Ko et al. 2003; Lin et al. 2005; Vršnak et al. 2009; Song et al. 2012; Guo et al. 2013; Webb & Vourlidas 2016) or SECCHI-COR2 (Song et al. 2012; Kwon et al. 2016; Chae et al. 2017) show that all observed post-CME blobs move outward with linear speeds from 126 to 1075 km s^{-1}. From these observational characteristics, it is generally believed that post-CME blobs observed by LASCO-C2 (or SECCHI-COR2) form within the heights from 1.0 to 2.0 $R_{\odot}$ (1.0 to 2.5 $R_{\odot}$) where the principle X-point of the magnetic reconnection regions is located.

In order to find out the formation heights of post-CME blobs observed by LASCO-C2 or SECCHI-COR2, several researchers have investigated the low coronal signatures of the post-CME blobs by using the *Solar Dynamics Observatory* (*SDO*; Pesnell et al. 2012)/Atmospheric Imaging Assembly (AIA; Lemen et al. 2012) data in multiple wavelengths (Schanche et al. 2016; Chae et al. 2017). Since they could not find any low coronal signatures corresponding to the post-CME blobs in EUV images, they suggested that the formation heights of post-CME blobs are higher than the AIA field of view (FOV). Recently, Cheng et al. (2018) examined the CS structure in the wake of a CME observed on 2017 September 10 by using K-Cor and *SDO*/AIA. They reported the following observational results: (1) The formation heights of eight post-CME blobs are near about 1.26 $R_{\odot}$, determined by examining K-Cor

running difference images with a Normalizing Radial Graded Filter (NRGF) technique (Morgan et al. 2006). (2) The formation heights of sunward outflow jets are near about 1.14 $R_\odot$, determined by investigating *SDO*/AIA 193 Å running difference images. By using the above formation heights of post-CME blobs and sunward outflow jets obtained from different wavelength observations, they suggest that the magnetic X-points of magnetic reconnection regions might be located at heights between 1.14 and 1.26 $R_\odot$.

There have been many studies on the possible formation mechanisms of the post-CME blobs by using resistivity magnetohydrodynamic (MHD) simulations (Riley et al. 2007; Shen et al. 2011; Mei et al. 2012; Guo et al. 2013). These studies commonly agree that the magnetic reconnection process is triggered by the tearing mode instability near the middle of post-CME CSs, which resemble Sweet–Parker CSs, that produce plasma blobs. The reconnection outflows generated by the magnetic reconnection processes near the magnetic X-points move the plasma blobs either upward or downward depending on their formation heights. By comparing post-CME blobs from LASCO-C2 observations and the MHD simulations, Guo et al. (2013) show that only large and bright post-CME blobs that have sizes larger than the spatial resolution of a coronagraph can be detected.

Since the K-Cor can observe inner corona structures from about 1.05 to 3.0 $R_\odot$ with a high spatial resolution (5.″5 pixel^{-1}) and a temporal cadence (15 s), it is suitable for investigating the origin and formation mechanism of post-CME blobs as well as their kinematics in the inner corona. In this study, by inspecting LASCO-C2 and K-Cor observations on 2017 September 10, we first show observational characteristics of two distinct types of inner corona blobs as well as sunward-moving blobs. In addition to that, we present clear observational evidence for the origin of outer corona blobs detected from LASCO-C2. We also present that the tearing mode instability inside a post-CME CS is a plausible formation mechanism for generating inner corona blobs.

This paper is organized as follows. In Section 2, we describe the data and the analyses to investigate observational characteristics of post-CME blobs. We provide our results in Section 3. A summary and discussion are presented in Section 4.

2. Data and Analysis

2.1. Data

In order to understand the origin and formation mechanism of LASCO-C2 post-CME blobs (hereafter, LASCO-C2 blobs), we investigate post-CME blobs along or in the post-CME CS after the eruption of a CME that was observed on 2017 September 10 (Cheng et al. 2018; Gary et al. 2018; Gopalswamy et al. 2018; Liu et al. 2018, 2019; Longcope et al. 2018). Its first appearance time is 16:00 UT. It is associated with an X8.2 class flare that occurred at 16:06 UT on the western limb. We inspect LASCO-C2 intensity images from 16:00 UT to 20:00 UT to identify the LASCO-C2 blobs. These LASCO-C2 images are taken from the *SOHO*/LASCO CME catalog[6], and LASCO-C2 produce corona structures from 2.0 to 6.0 $R_\odot$ with a spatial resolution of 23″ pixel^{-1} and a temporal cadence of 12 minutes. For identifying the inner corona blob structures associated with the LASCO-C2 blobs, we use K-Cor level-1.5 pB data, which includes fully calibrated polarization brightness (pB) of the K-Corona, during the observational period from 17:11 UT to 20:20 UT. K-Cor data are taken from the K-Cor online database.[7]

2.2. LASCO-C2 Blobs and Their Locations

As shown in Figure 1, outward-moving localized brightness structures along the post-CME CS formed in the wake of a CME are called post-CME blobs. To identify the LASCO-C2 blobs and determine their locations, we use the following procedure: (1) By visual inspection of each LASCO-C2 intensity images, we find localized brightness enhancement structures. (2) When the localized brightness structures moving outward are observed in at least three consecutive images, we select them as candidates of LASCO-C2 blobs. (3) To determine the locations of LASCO-C2 blobs, we choose their local maximum brightness positions in LASCO-C2 intensity images. In addition to that, we measure the front, trailing, and lateral edges of the LASCO-C2 blobs to estimate their morphological features. Since it is hard to find the candidates of LASCO-C2 blobs due to the appearance of solar energetic particles as shown in the bottom panels of Figure 1, we can identify the LASCO-C2 blobs before 18:48 UT. To estimate the times and locations of LASCO-C2 post-CME blobs, we use the height–time measurement tool provided by the *SOHO*/LASCO CME catalog.[8] By using this tool, we can study coronal structures at heights from 2.2 to 6.0 $R_\odot$ with a spatial resolution of 46″ pixel^{-1}. Since the measurement uncertainty for the determination of LASCO-C2 blob locations, as deduced from 10 measurements of a blob position in the height–time measurement tool, is about 0.1 $R_\odot$ (about 2 pixel sizes), we simply assume 0.1 $R_\odot$ as the measurement uncertainty.

By using the above analysis, we find four LASCO-C2 blobs as shown in Figure 1. We estimate their appearance heights during the durations, which are shown in the fourth column of Table 1. Here, the appearance heights are measured from the center of the Sun. By applying the first- and second-order polynomial fits to the time-height data of the LASCO-C2 blobs, we determine their linear speeds and average accelerations, which are shown in the fifth and sixth columns. The values in parentheses are the measurement errors for the determinations of the linear speeds and the accelerations, which are estimated from the first- and second-order polynomial fitting with the measurement uncertainties for the determinations of blob locations. We also measure their average lateral widths, radial widths, aspect ratios (lateral widths to radial widths), which are presented in the seventh, eighth, and ninth columns. Here, the lateral widths are the difference between lateral edges and radial widths are the difference between front and trailing edges. Their standard deviations are also presented.

When we examine the LASCO-C3 intensity images, we also find four LASCO-C3 blobs during the observational period from 16:00 to 20:00 UT. The LASCO-C3 blobs first appear at 16:54, 17:18, 18:18, and 18:30 UT at the heights of 4.2, 4.9, 4.5, and 4.2 $R_\odot$, respectively. These blobs are spatially and temporally correlated with the LASCO-C2 blobs. We notice that it is hard to identify the post-CME CS structure in the wake

[6] http://cdaw.gsfc.nasa.gov/CME_list/

[7] https://mlso.hao.ucar.edu/mlso_data_summary.php?date=2017-09-10&inst=kcor

[8] https://cdaw.gsfc.nasa.gov/movie/make_htmem_js.php?step=1&img1=lasc2aia193&stime=20170910_0000&etime=20170910_2359

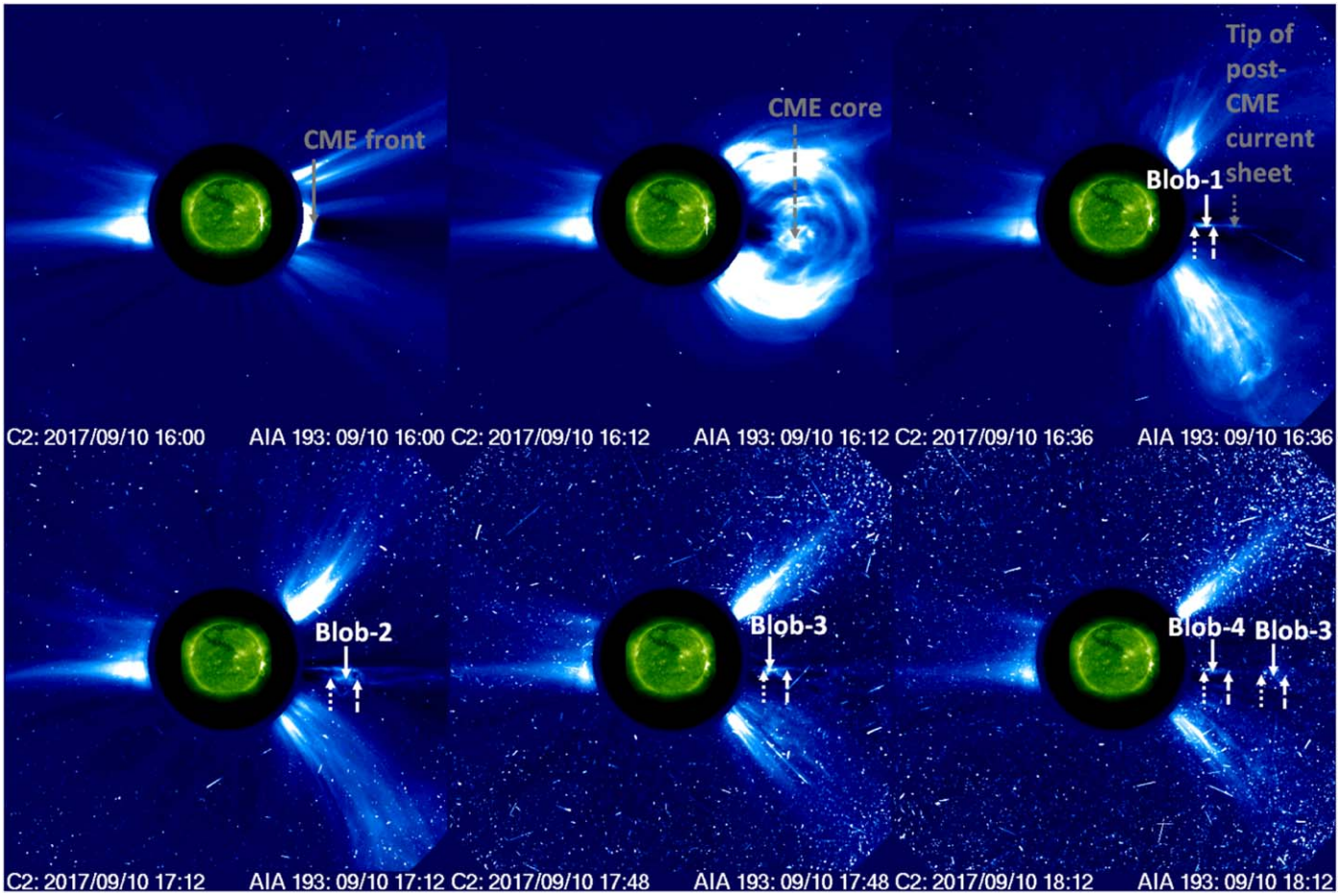

Figure 1. Time sequence of LASCO-C2 combined with *SDO*/AIA 193 Å intensity images observed on 2017 September 10 from 16:00 UT to 18:12 UT. The ray arrow, the dashed arrow, and the dotted arrow represent the CME front, CME core, and tip of post-CME CS, respectively. "Blob-1," "Blob-2," "Blob-3" and "Blob-4" indicate LASCO-C2 post-CME blobs. White solid, dashed, and dotted arrows show the local maximum brightness, front edge, and trailing edge positions of post-CME blobs, respectively. The black circle indicates the location and size of the LASCO-C2 occulting disk.

Table 1
Observational Characteristics of Four LASCO-C2 Blobs on 2017 September 10 from 16:36 to 18:48 UT

Blob	First appearance time	Final appearance time	Appearance height during a duration	Linear speed (measurement error)	Average acceleration (measurement error)	Average lateral width with standard deviation	Average radial width with standard deviation	Average aspect ratio (lateral width/radial width) with standard deviation	Estimated appearance time in K-Cor FOV
	(UT)	(UT)	($R_\odot$)	(km s^{-1})	(m s^{-2})	($R_\odot$)	($R_\odot$)		(UT)
(1)	(2)	(3)	(4)	(5)	(6)	(7)	(8)	(9)	(10)
1	16:36	17:00	2.62 ∼ 4.65	977 (±68)	43 (±328)	0.14 ± 0.01	0.60 ± 0.09	0.23 ± 0.03	16:17 ∼ 16:36
2	17:00	17:24	2.53 ∼ 4.41	908 (±68)	55 (±328)	0.30 ± 0.16	0.99 ± 0.64	0.31 ± 0.10	16:41 ∼ 17:00
3	17:36	18:24	2.32 ∼ 5.50	787 (±30)	197 (±72)	0.35 ± 0.14	0.68 ± 0.17	0.54 ± 0.28	17:17 ∼ 17:36
4	18:12	18:48	2.69 ∼ 5.09	767 (±43)	−154 (±134)	0.21 ± 0.03	0.53 ± 0.19	0.46 ± 0.25	17:47 ∼ 18:12

of the CME as shown in the bottom panels of Figure 1, which is different from previous observations (Ko et al. 2003; Lin et al. 2005; Riley et al. 2007; Song et al. 2012; Guo et al. 2013). From this observational characteristic, we suppose that the formation location of the post-CME CS is lower than LASCO-C2 FOV.

2.3. K-Cor Blobs Associated with the LASCO-C2 Blobs

Assuming that post-CME blobs move outward with constant speeds and they form below LASCO-C2 FOV, we can estimate the appearance times of post-CME blobs in K-Cor FOV, which are shown in the tenth column of Table 1. Since the K-Cor

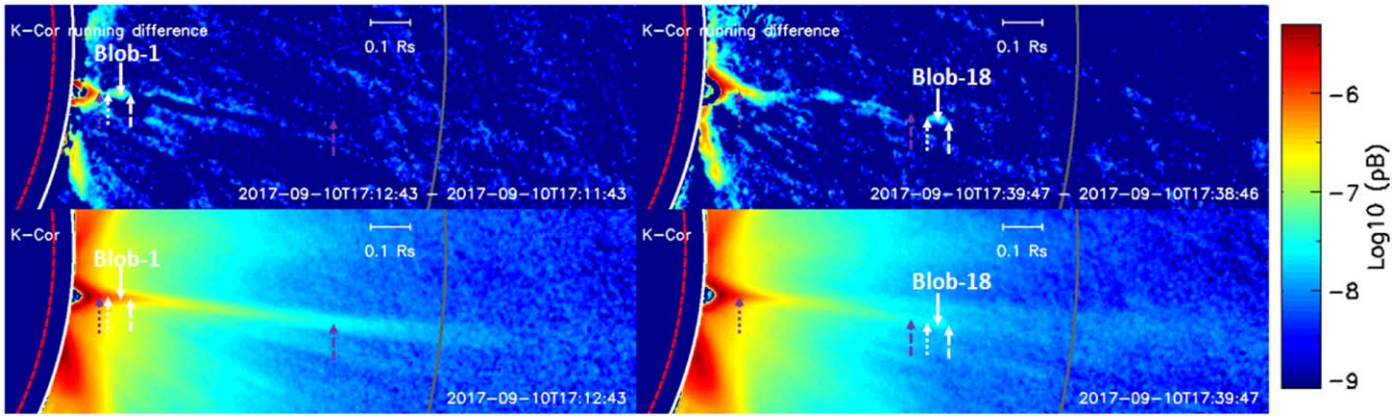

Figure 2. Examples of K-Cor blobs appeared in the post-CME CS (left column) and above the tip of the CS (right column), which are observed on 2017 September 10 at 17:12:43 UT and at 17:39:47 UT, respectively. Top and bottom panels show K-Cor running difference and intensity images, which are cut as XCEN and YCEN are 1615″ and −152″ while the FOV is 1531″ and 504″. "Blob-1" and "Blob-18" indicate the K-Cor blobs. The purple dashed–dotted arrows show the tips of post-CME CS and post-flare arcades, respectively. The red dashed and white partial circles represent the location and size of the solar disk and the K-Cor occulting disk. The gray partial circles indicate the estimated locations and size of the LASCO-C2 occulting disk with a radius of 2.0 $R_{\odot}$. The white solid, dashed, and dotted arrows are the same as those in Figure 1.

observe inner corona structures from 17:11 to 20:20 UT on 2017 September 10, we can attempt to search the K-Cor blobs associated with LASCO-C2 "Blob-3" and "Blob-4."

To find the K-Cor blobs associated with LASCO-C2 "Blob-3" and "Blob-4," we take the following procedure: (1) We plot K-Cor intensity images and their running difference images with an interval of 1 minute. (2) By using the K-Cor images, we identify K-Cor blobs and their locations. For selecting the K-Cor blobs, we adopted the criteria that localized brightness enhancement structures are observed in at least four consecutive images and they move outward. Since the pixel size of a K-Cor image is 5.″5, we simply assume about 0.01 $R_{\odot}$ (about 2 pixel sizes) as the measurement uncertainty of the blob locations. (3) We investigate whether or not the selected K-Cor blobs exist within the estimated appearance time windows. From this, we can determine the candidates of K-Cor blobs associated with LASCO-C2 "Blob-3" and "Blob-4" (4) Finally, we find the inner corona counter parts of LASCO-C2 "Blob-3" and "Blob-4" by comparing the height–time data between LASCO-C2 and K-Cor blobs.

We also investigate observational characteristics of K-Cor blobs. By visual inspection of post-CME CS and K-Cor blob locations in K-Cor intensity and running difference images, we examine the formation regions of K-Cor blobs. By investigating their height–time data, we also estimate kinematics such as durations, propagations, linear speeds, and average accelerations.

2.4. Formation Mechanism of K-Cor Blobs

It is generally believed that post-CME blobs are generated by a magnetic reconnection process triggered by the tearing mode instability in the Sweet–Parker CSs (Furth et al. 1963; Shibata & Tanuma 2001; Riley et al. 2007; Shen et al. 2011; Mei et al. 2012; Guo et al. 2013; Takahashi et al. 2017). Furth et al. (1963) find that if the length of the CS is about six times longer than its width, the CSs spontaneously reconnect to make a set of magnetic islands because the CSs are unstable to the linear tearing mode. In addition to that, several simulation results show that post-CME blobs generated by the tearing mode instability are formed near the middle of the CS (Shen et al. 2011; Mei et al. 2012; Guo et al. 2013; Takahashi et al. 2017). In particular, Mei et al. (2012) and Takahashi et al. (2017) show that the lateral widths of post-CME blobs are smaller than those of post-CME CS structures. Mei et al. (2012) report that post-CME blobs have elongated shapes whose ratios of lateral widths to radial widths are about 0.5 during the simulation periods. It should be noted that the impact of the linear tearing mode instability on the magnetic reconnection process might be limited because elaborate studies by numerical experiments have shown that the value (the ratio of the length of a CS to its width) needs to be above 50 in order to develop tearing mode instability (Ni & Lukin 2018).

To examine the possibility that observed K-Cor blobs are generated by the tearing mode instability inside a post-CME CS, we check three observational characteristics: (1) the linear tearing mode instability condition of the post-CME CS, (2) morphological features of the blobs, and (3) their formation regions. To check the tearing mode instability condition, we measure the radial lengths and lateral widths of the CS during the K-Cor observations, and estimate the ratios of radial lengths to lateral widths. We compare our estimates with the linear tearing mode instability condition from Furth et al. (1963). To confirm the morphological features, we measure the lateral widths of K-Cor blobs and compare them with the lateral widths of the CS structures. We also estimate the ratios of lateral widths to radial widths of the blobs and compare our estimates with those from Mei et al. (2012). To investigate the formation regions, we compare the locations of the CS with those of K-Cor blobs at their first appearance times.

3. Results

By investigating K-Cor observations from 17:11 to 20:20 UT on 2017 September 10, we find 34 K-Cor blobs in or along a post-CME CS. We also find that the post-CME CS structure is well detected in the K-Cor. Examples of the observed K-Cor blobs and the CS structure are presented in Figure 2. Among 34 K-Cor blobs, 27 blobs are identified in the heights above the post-flare arcades as shown in the top left panel of Figure 2. When we examine the formation regions of 27 blobs, we find that all blobs are located in the CS (hereafter, Group 1) as shown in the bottom left panel of the Figure 2. The other 7 blobs appear in the heights near or above the tips of the CS (hereafter, Group 2) as shown in the bottom right panel of

Table 2
Observational Characteristics of 34 K-Cor Blobs on 2017 September 10 from 17:11 UT to 18:58 UT

Blob	First appearance time	Final appearance time	Appearance height during a duration	Linear speed	Average acceleration	Average lateral width	Average radial width	Average aspect ratio (lateral width/ radial width)	Group (1/2)
	(UT)	(UT)	($R_\odot$)	(km s^{-1})	(m s^{-2})	($R_\odot$)	($R_\odot$)		
(1)	(2)	(3)	(4)	(5)	(6)	(7)	(8)	(9)	(10)
1	17:12:43	17:13:44	1.19 ∼ 1.22	258 (±174)	−1,390 (±19,080)	0.03 ± 0.00	0.06 ± 0.01	0.56 ± 0.13	1
2	17:12:59	17:15:30	1.37 ∼ 1.51	674 (±53)	243 (±2,502)	0.02 ± 0.01	0.05 ± 0.01	0.51 ± 0.19	1
3	17:15:00	17:16:31	1.27 ∼ 1.29	151 (±104)	9,730 (±7,937)	0.02 ± 0.00	0.06 ± 0.02	0.39 ± 0.08	1
4	17:15:00	17:16:31	1.34 ∼ 1.38	263 (±104)	−695 (±7,937)	0.02 ± 0.01	0.05 ± 0.01	0.31 ± 0.12	1
5	17:20:03	17:22:20	1.36 ∼ 1.45	423 (±61)	695 (±3,133)	0.02 ± 0.01	0.04 ± 0.01	0.47 ± 0.13	1
6	17:20:03	17:22:20	1.52 ∼ 1.62	566 (±61)	−695 (±3,133)	0.03 ± 0.01	0.05 ± 0.02	0.61 ± 0.26	1
7	17:20:03	17:22:20	1.65 ∼ 1.73	408 (±61)	202 (±3,133)	0.03 ± 0.01	0.05 ± 0.01	0.65 ± 0.20	1
8	17:23:05	17:23:51	1.30 ∼ 1.33	208 (±244)	−34,055 (±35,294)	0.03 ± 0.01	0.05 ± 0.01	0.48 ± 0.21	1
9	17:23:05	17:23:51	1.40 ∼ 1.45	635 (±244)	14,595 (±35,294)	0.02 ± 0.01	0.06 ± 0.02	0.39 ± 0.21	1
10	17:23:05	17:25:22	1.51 ∼ 1.64	655 (±61)	5,560 (±3,133)	0.02 ± 0.01	0.04 ± 0.01	0.59 ± 0.18	1
11	17:24:36	17:26:07	1.24 ∼ 1.29	386 (±104)	4,865 (±7,898)	0.02 ± 0.01	0.05 ± 0.01	0.47 ± 0.14	1
12	17:28:09	17:31:26	1.29 ∼ 1.44	526 (±36)	1,390 (±1,344)	0.02 ± 0.01	0.04 ± 0.01	0.49 ± 0.22	1
13	17:28:54	17:31:41	1.19 ∼ 1.26	326 (±46)	695 (±1,980)	0.02 ± 0.00	0.04 ± 0.01	0.49 ± 0.22	1
14	17:30:56	17:36:45	1.95 ∼ 2.31	699 (±30)	1,390 (±542)	0.05 ± 0.03	0.21 ± 0.06	0.28 ± 0.13	2
15	17:31:56	17:39:47	1.71 ∼ 2.09	579 (±19)	−695 (±295)	0.07 ± 0.04	0.13 ± 0.04	0.48 ± 0.22	2
16	17:32:57	17:34:13	1.24 ∼ 1.28	462 (±131)	6,255 (±11,878)	0.02 ± 0.01	0.06 ± 0.02	0.40 ± 0.20	1
17	17:37:00	17:42:49	1.28 ∼ 1.74	945 (±16)	−695 (±346)	0.03 ± 0.01	0.06 ± 0.01	0.58 ± 0.17	1
18	17:37:45	17:42:49	1.57 ∼ 1.87	713 (±20)	695 (±483)	0.02 ± 0.01	0.05 ± 0.01	0.45 ± 0.16	2
19	17:39:16	17:42:49	1.38 ∼ 1.54	562 (±33)	2,085 (±1,122)	0.03 ± 0.01	0.05 ± 0.01	0.59 ± 0.19	1
20	17:40:47	17:41:33	1.23 ∼ 1.24	38 (±244)	11,815 (±35,294)	0.02 ± 0.01	0.04 ± 0.01	0.54 ± 0.33	1
21	17:48:07	17:50:39	1.33 ∼ 1.44	460 (±52)	3,475 (±2456)	0.02 ± 0.01	0.03 ± 0.01	0.59 ± 0.21	1
22	17:49:53	17:55:58	1.76 ∼ 2.12	726 (±26)	−236 (±491)	0.04 ± 0.01	0.13 ± 0.03	0.33 ± 0.08	2
23	17:54:57	17:59:00	1.77 ∼ 1.97	624 (±44)	2,085 (±1,207)	0.05 ± 0.02	0.12 ± 0.03	0.43 ± 0.08	2
24	17:59:45	18:01:16	1.21 ∼ 1.27	374 (±104)	6,950 (±7,937)	0.03 ± 0.01	0.05 ± 0.01	0.56 ± 0.22	1
25	18:00:00	18:07:05	1.81 ∼ 2.18	621 (±21)	139 (±349)	0.05 ± 0.01	0.14 ± 0.04	0.39 ± 0.12	2
26	18:04:03	18:08:21	1.40 ∼ 1.64	660 (±25)	2,780 (±711)	0.02 ± 0.01	0.05 ± 0.01	0.47 ± 0.15	1
27	18:08:51	18:15:11	1.43 ∼ 1.83	748 (±14)	695 (±19,262)	0.03 ± 0.01	0.04 ± 0.01	0.63 ± 0.22	1
28	18:10:07	18:12:24	1.19 ∼ 1.23	182 (±60)	2,780 (±3122)	0.03 ± 0.01	0.06 ± 0.01	0.53 ± 0.11	1
29	18:23:31	18:24:32	1.19 ∼ 1.20	66 (±172)	−1,390 (±3,183)	0.02 ± 0.01	0.04 ± 0.02	0.68 ± 0.21	1
30	18:24:17	18:30:21	1.72 ∼ 2.07	647 (±26)	2,780 (±494)	0.05 ± 0.01	0.13 ± 0.05	0.45 ± 0.14	2
31	18:31:37	18:35:09	1.27 ∼ 1.38	343 (±33)	−695 (±1,131)	0.02 ± 0.01	0.06 ± 0.01	0.45 ± 0.15	1
32	18:32:53	18:35:09	1.38 ∼ 1.51	692 (±61)	−1,390 (±3,183)	0.03 ± 0.01	0.06 ± 0.01	0.57 ± 0.16	1
33	18:38:57	18:40:12	1.17 ∼ 1.19	234 (±133)	2,085 (±12,133)	0.02 ± 0.01	0.04 ± 0.01	0.50 ± 0.14	1
34	18:51:50	18:55:38	1.25 ∼ 1.38	348 (±31)	−695 (±963)	0.03 ± 0.01	0.04 ± 0.01	0.59 ± 0.20	1

Figure 2. Since the structures of K-Cor blobs of Group 2 are more clearly identified in the K-Cor intensity images than in K-Cor running difference ones, except for one blob ("Blob-18," as shown in the right panel of Figure 2), we determine their locations and structures by using K-Cor intensity images. The observational characteristics of 34 K-Cor blobs are summarized in Table 2. Their appearance heights, linear speeds, and average accelerations during the durations are shown in the fourth, fifth, and sixth columns. Their average lateral widths, radial widths, and aspect ratios are presented in the seventh, eighth, and ninth columns. In the tenth column, 1 and 2 indicate the post-CME blobs are located in the post-CME CS and above the tips of the CS, respectively.

3.1. Two Distinct Types of Inner Corona Blobs

The top and bottom panels of Figure 3 show the height–time plot for observed 34 K-Cor blobs with overlaying images showing the spacetime plots of K-Cor intensity and running difference images along the direction of the post-CME CS. From this, we find that Groups 1 and 2 have different observational characteristics: (1) Group 1 (orange color symbols) is clearly formed below the tips of the post-CME CS, its heights range from 1.5 to 1.8 $R_\odot$, and Group 2 (green color symbols) appears near or above it. (2) The first appearance time of Group 2 (K-Cor "Blob-14") is 17:30:56 UT, which is about 18 minutes later than the first appearance time of Group 1 (K-Cor "Blob-1"). (3) Only Group 1 has multiple blob

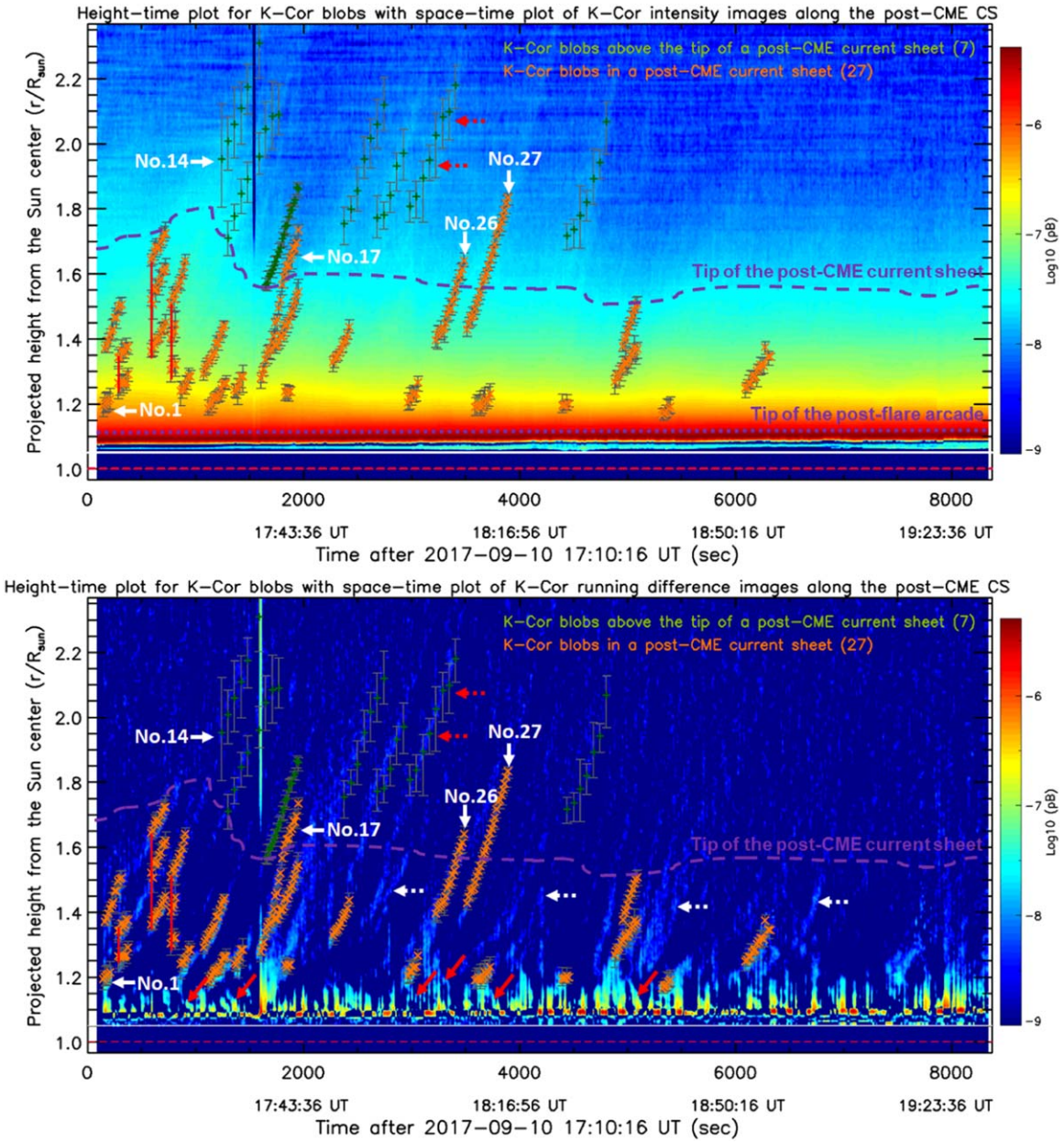

Figure 3. Height–time plot for 34 K-Cor blobs overlapped with spacetime plots of K-Cor intensity (top) and running difference images (bottom) along the direction of the post-CME CS. Orange and green symbols indicate K-Cor blobs detected in the post-CME CS (Group 1) and near or above the tips of the CS (Group 2), respectively. The gray vertical error bars indicate the observation heights for the front and trailing edges of each K-Cor blob. Purple dashed and dotted lines indicate the locations of the tips of the CS and post-flare arcades, respectively. Three red vertical lines at 17:15:00 UT, 17:20:03 UT, and 17:23:05 UT, indicate the first appearance times for multiple blobs with different heights. Red dashed and white horizontal lines show the size of the solar disk and the K-Cor occulting disk, respectively. Red dotted arrows show examples of the overestimation of blob sizes by visual inspection of K-Cor intensity images. In the bottom panels, white dotted and red arrows indicate the candidates of K-Cor blobs and sunward-moving blobs, respectively.

formations with different heights at the same times as denoted by the red vertical lines. (4) Group 1 has shorter lifetimes (Group $1 = \langle 145\mathrm{s} \rangle$; Group $2 = \langle 360\mathrm{s} \rangle$), lower initial appearance heights (Group $1 = \langle 1.34 R_\odot \rangle$; Group $2 = \langle 1.78 R_\odot \rangle$), lower final appearance heights (Group $1 = \langle 1.45 R_\odot \rangle$; Group $2 = \langle 2.11 R_\odot \rangle$), smaller lateral widths (Group $1 = \langle 0.024 R_\odot \rangle$; Group $2 = \langle 0.047 R_\odot \rangle$), and smaller radial widths (Group $1 = \langle 0.049 R_\odot \rangle$; Group $2 = \langle 0.130 R_\odot \rangle$) than those of Group 2. These results first demonstrate that inner corona blobs are persistently formed in the post-CME CS. The other blobs consistently occurred near or above the tips of the CS after the formation and propagation of the inner corona blobs. It is noted that the sizes of Group 1 are smaller than those of Group 2. The difference in the size of the blob might result from the difference in the location where the blob appears: at lower heights, both the magnetic and gas pressures are higher, so the size of the blob is suppressed; and at higher heights, both the magnetic and gas pressures are lower, so the size of the blob is able to grow more easily. We also note that Group 1 tends to suddenly disappear without merging with each other. These might be related to the fact that in the magnetized plasma, the smaller the structure is, the more easily it is diffused. Regarding propagations of Group 1, we find that among the 27 K-Cor blobs, 23 are located in the post-CME CS and only 3 blobs (Nos. 17, 26, and 27 in Table 2) propagate above the tip of the CS. This indicates that post-CME

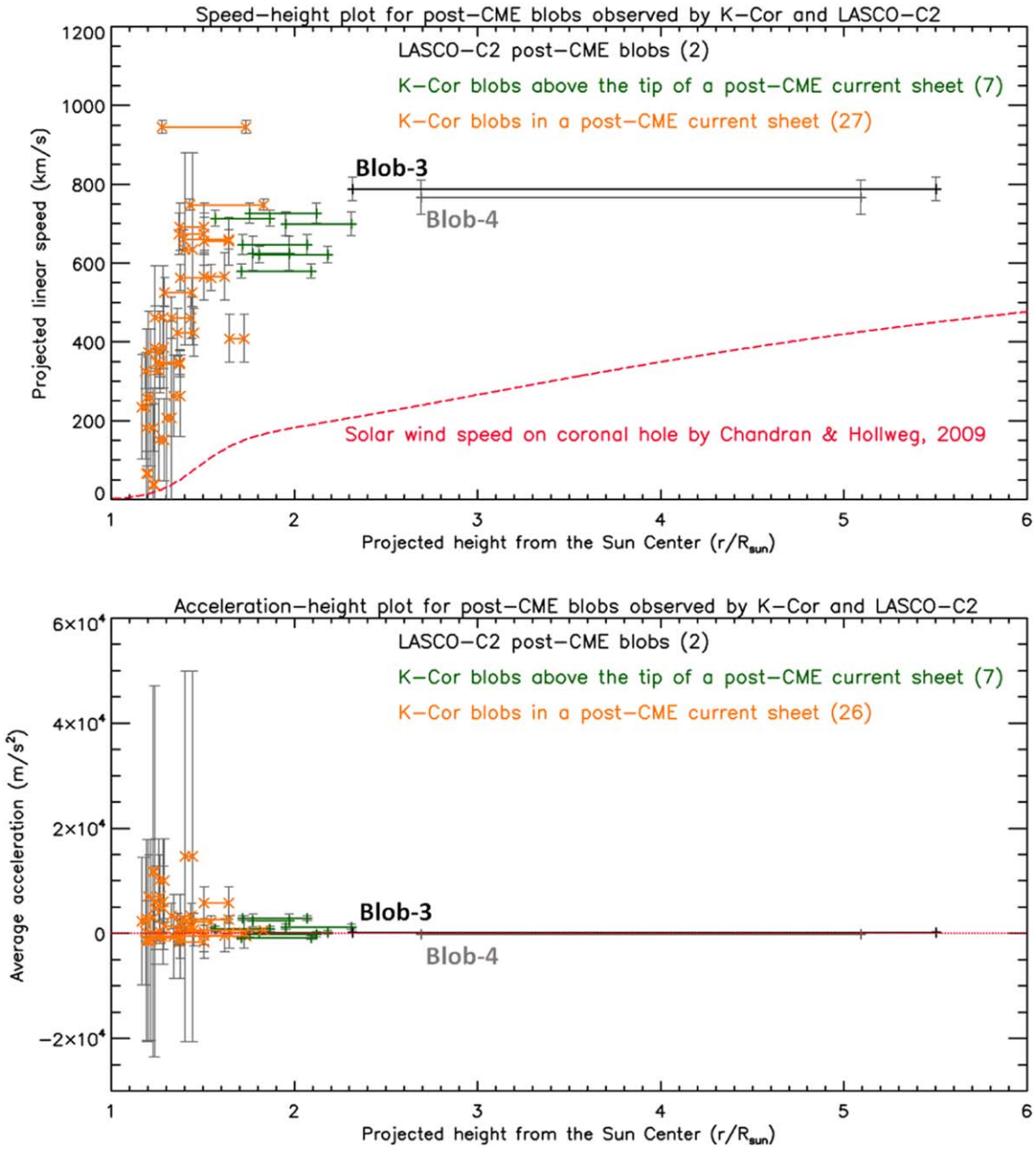

Figure 4. Speed–height plot (top panel) and acceleration–height plot (bottom panel) for 34 K-Cor blobs and 2 LASCO-C2 blobs. In the top panel (bottom panel), black plus symbols with lines represent the linear speeds (average accelerations) of the local maximum brightness positions of LASCO-C2 blobs. Symbols based on orange colors and green colors indicate the linear speeds (average accelerations) of K-Cor blobs detected in the post-CME CS and above the tip of the CS. First and second symbols of each blob show their initial and final appearance heights. The gray vertical error bars show the measurement uncertainties for the determination of the linear speeds (average accelerations) of each of the blobs, which are estimated from the first- and second-order polynomial fittings with the measurement uncertainties for the determination of each selected blob location. The red line shows the solar wind speed based on coronal hole given by Chandra & Hollweg (2009; zero average acceleration). In the bottom panel, we do not display one blob (No. 8), which has an extremely large deceleration of $-34{,}055$ m s^{-2}.

blobs that formed in the post-CME CS have difficulty escaping from the CS.

Figure 4 shows speed–height and acceleration–height plots for 34 K-Cor blobs and 2 LASCO-C2 blobs. From this, we also find that Groups 1 and 2 have different kinematics: (1) Group 1 has a broad linear speed range (38 $\sim$ 945 km s^{-1}) and its linear speed distribution tends to increase dramatically from 38 to 945 km s^{-1} (748 km s^{-1}) at the heights between about 1.17 and 1.74 $R_\odot$ (or 1.83 $R_\odot$) as shown by orange symbols in the top panel. On the other hand, Group 2 has a constant speed with a narrow range between 579 and 726 km s^{-1} as denoted by green symbols. We also find that Group 2 has similar kinematics with LASCO-C2 blobs whose speeds range from 767 to 787 km s^{-1} as represented by black symbols. (2) Regarding accelerations, Group 1 has larger average accelerations (Group 1 $= \langle 4272$ ms$^{-2}\rangle$; Group 2 $= \langle 1418$ ms$^{-2}\rangle$) than those of Group 2 as shown in the bottom panel. Our results indicate that inner corona blobs form in the post-CME CS and undergo a larger acceleration process than those formed above the tips of the CS, which might cause their linear speed distributions. We notice that the linear speed distributions of K-Cor blobs and LASCO-C2 blobs are much

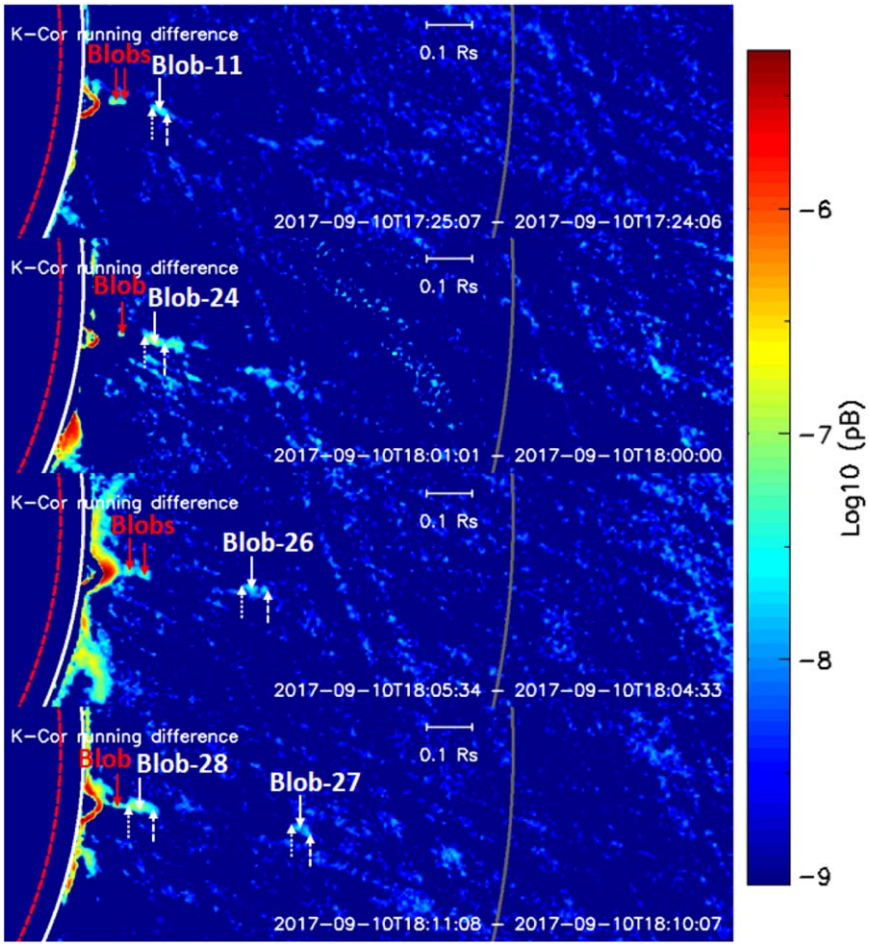

Figure 5. K-Cor running difference images observed on 2017 September 10 at 17:25:07, 18:01:01, 18:05:34, and 18:11:08 UT. Red and white "Blob" indicate the candidates of sunward-moving blobs and outward-moving blobs, respectively. The red arrows indicate the local maximum brightness of sunward-moving blobs. The white solid, dashed, and dotted arrows are the same as those in Figure 1. The red, white, gray, and gray dashed partial circles are the same as those in Figure 2.

higher than the solar wind speed on the coronal hole given by Chandra & Hollweg (2009) shown by the red dashed line. This implies that a post-CME CS might be the origin of a fast solar wind if reconnection outflows generated by the magnetic reconnection processes near the magnetic X-points move post-CME blobs outward. We also note that about 68% (23/34) of K-Cor blobs (18 blobs of Group 1 and 5 blobs of Group 2) undergo an acceleration process as shown in the time-height plot of Blob No. 26 in Figure 3, while the other blobs (32%, 11/34, 9 blobs of Group 1 and 2 blobs Group 2) undergo a deceleration process as shown in that of Blob No. 1. This indicates that the speeds of inner corona blobs tend to be increased or decreased with time during their propagations.

3.2. Sunward-moving Blobs

We carefully examine the trajectories of inner corona blobs observed in the spacetime plots of K-Cor running difference images along the post-CME CS (bottom panel of Figure 3). From this, we find that there are more candidates of K-Cor blobs as represented by white dotted arrows. We also find the six candidates of sunward-moving inner corona blobs as denoted by red arrows. When we investigate six candidates of the sunward-moving blobs by using our visual inspection, we find that among six candidates, four have blob structures at the specific times shown in Figure 5. Their appearance heights range from 1.14 to 1.21 $R_\odot$ (Mean = 1.17 $R_\odot$). Their ratios of lateral widths to radial widths range from 0.50 to 1.00 (Mean = 0.86), representing that sunward-moving blobs have circular shapes. In addition to that, we find that the heights of outward-moving blobs range from 1.20 to 1.43 $R_\odot$ (Mean = 1.26 $R_\odot$). Our results first demonstrate that sunward-moving blobs are persistently formed in the bottoms of the post-CME CS, and magnetic X-points of magnetic reconnection regions are located near the heights between 1.17 $R_\odot$ and 1.26 $R_\odot$. It is noted that we cannot trace the sunward-moving blobs because they are detected at specific times. This may be due to a change of their brightness by a magnetic reconnection or a rapid propagation of the blobs to post-flare arcades.

3.3. Two Kinds of Tearing Mode Instability for Generating Inner Corona Blobs

We examine whether or not observed K-Cor blobs can be generated by the tearing mode instability inside the post-CME CS. For this, we check three observational characteristics: (1) the linear tearing mode instability condition of the post-CME CS, (2) the morphological features of K-Cor blobs, and (3) their formation regions. First, we check the tearing mode instability condition of the CS. For this, we estimate its ratios of radial length to lateral width during the K-Cor observation period. Here, radial lengths are the differences of the tips between the

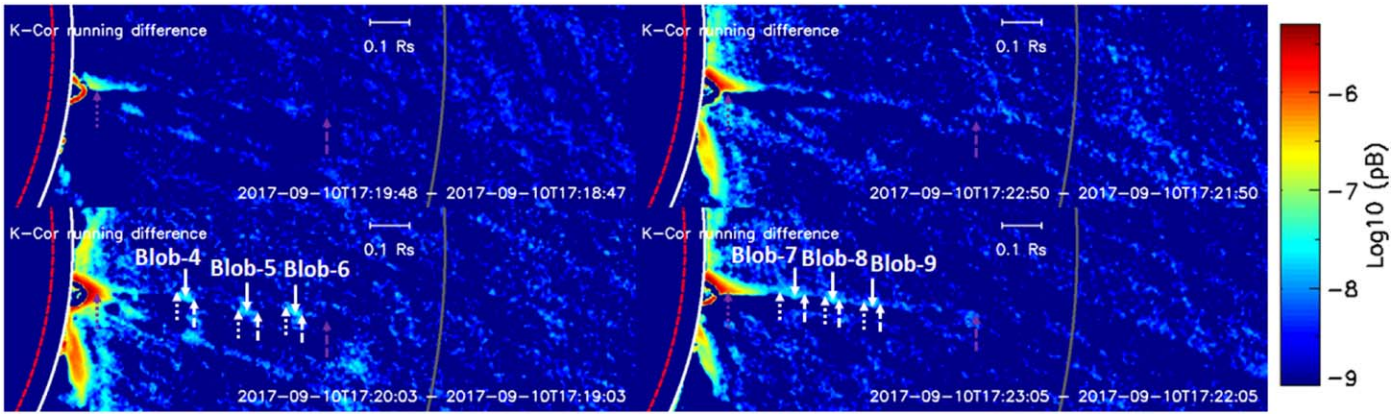

Figure 6. Time sequence of K-Cor running difference images observed on 2017 September 10 from 17:19:48 to 17:20:03 UT (left column) and K-Cor running difference images from 17:22:50 to 17:23:05 UT (right column). "Blob" indicates the K-Cor blobs in the post-CME CS. The white solid, dashed, and dotted arrows are the same as those in Figure 1. The red dashed, white, gray, and gray dashed partial circles, and purple dashed and dotted arrows are the same as those in Figure 2.

CS and post-flare arcades as represented by purple dashed and dotted lines in Figure 3. We find that the radial lengths range from 0.40 $R_\odot$ to 0.63 $R_\odot$ (Mean = 0.51 $R_\odot$) and the lateral widths range from 0.04 $R_\odot$ to 0.07 $R_\odot$ (Mean = 0.06 $R_\odot$). The ratios range from 6.29 to 15.75 (Mean = 9.38 $R_\odot$), which are larger than the liner tearing mode instability condition (about 6) from Furth et al. (1963). These results indicate that the post-CME CS is unstable to the linear tearing mode.

Second, we confirm the morphological features of Groups 1 and 2. For this, we measure the average lateral widths of each blob shown in the sixth column of Table 2. We find that the lateral widths of Group 1 range from 0.02 to 0.03 (Mean = 0.02), which are smaller than the lateral widths of post-CME CS structures. On the other hand, Group 2 has the lateral width range from 0.02 to 0.07 (Mean = 0.05), which is similar to those of the CS structures. In addition to that, we estimate average aspect ratios of each blob shown in the eighth column of Table 2. We find that the ratios of Group 1 range from 0.31 to 0.68 (Mean = 0.52), which is similar to those from the MHD simulation Mei et al. (2012). On the other hand, Group 2 has the ratio range from 0.28 to 0.48 (Mean = 0.40), which is smaller to those from the MHD simulation. These results imply that the inner corona blobs that appeared in the post-CME CS have elongated shapes and they might be generated by the tearing mode instability inside the CS. The other blobs observed above tips of the CS might be generated by another formation mechanism related to tearing mode instability. It should be noted that our visual inspection with K-Cor intensity images tends to overestimate blob sizes as represented by red dotted arrows in Figure 3. This might cause the lateral widths and aspect ratios of Group 2 to be overestimated and underestimated. Therefore, all inner corona blobs might be generated by same tearing mode instability inside the post-CME CS.

Third, we carefully investigate the formation regions of the K-Cor blobs at their first appearance times. Figures 6 and 7 show examples of Groups 1 and 2. From this, we find that Groups 1 and 2 have different observational characteristics: all blobs of Group 1 suddenly appear in the post-CME CS while all blobs of Group 2 appear on the tips of the CS as shown in Figures 6 and 7. Before the appearances of blobs of Group 2, localized brightness enhancement structures appear near the tips of the CS and are indicated by dark blue arrows in the second and third panels of Figure 7. The blobs of Group 2 occur in the tip of the shrinking CS as denoted by red arrows in the bottom panels. These results together with the above findings (the linear tearing mode instability condition of the post-CME CS and morphological features of K-Cor blobs) demonstrate that inner corona blobs formed in the post-CME CS are generated by the magnetic reconnection process triggered by the tearing mode instability near the middle of the Sweet–Parker CS (Shibata & Tanuma 2001; Shen et al. 2011; Takahashi et al. 2017). The other blobs that appeared above the tips of the CS are caused by the tearing mode instability near the tip of the CS as shown in Figure 5 of Sitnov et al. (2002). They explain that the magnetic reconnection process triggered by the tearing mode instability can happen near extremely stretched magnetic field lines in the tail of Earth's magnetosphere because the length of the tail CS is much larger than its thickness.

3.4. Origin and Formation Mechanism of Outer Corona Blobs

Figure 8 shows the height–time plot for 34 K-Cor blobs and 2 LASCO-C2 blobs. We find the observational results: (1) Among 12 K-Cor blobs within the estimated time window (red dotted vertical lines), only one blob of Group 2 is spatially associated with the LASCO-C2 "Blob-3" near the time of 17:36 UT. This inner corona blob moves outward from the height of 1.95 to 2.31 $R_\odot$ from 17:30:56 to 17:36:45 UT. (2) Among 8 candidates (blue dotted vertical lines) that may be associated with LASCO-C2 "Blob-4," only one blob of Group 2 might be related to the LASCO-C2 "Blob-4." This blob moves outward from the height of 1.81 $R_\odot$ to 2.18 $R_\odot$ from 18:00:00 UT to 18:07:05 UT. Our results together with the formation mechanism of Group 2 as described in Section 3.3 first demonstrate that LASCO-C2 blobs are generated by the tearing mode instability near the tips of the post-CME CS whose heights from 1.5 to 1.8 $R_\odot$. It is noted that many of the inner corona blobs above the tips of the CS cannot be identified in the outer corona (LASCO-C2 FOV) even though they do not seem to be merged with each other as shown in Figures 3 and 8. These might be related to the low time cadence of LASCO-C2 causing some of the blobs observed by K-Cor with high time cadence to be missed by LASCO-C2. In addition to that, we cannot rule out the possibilities of their expansions or perpendicular propagations in the plane of the sky that reduce their brightness below the brightness sensitivities of the LASCO-C2 instrument.

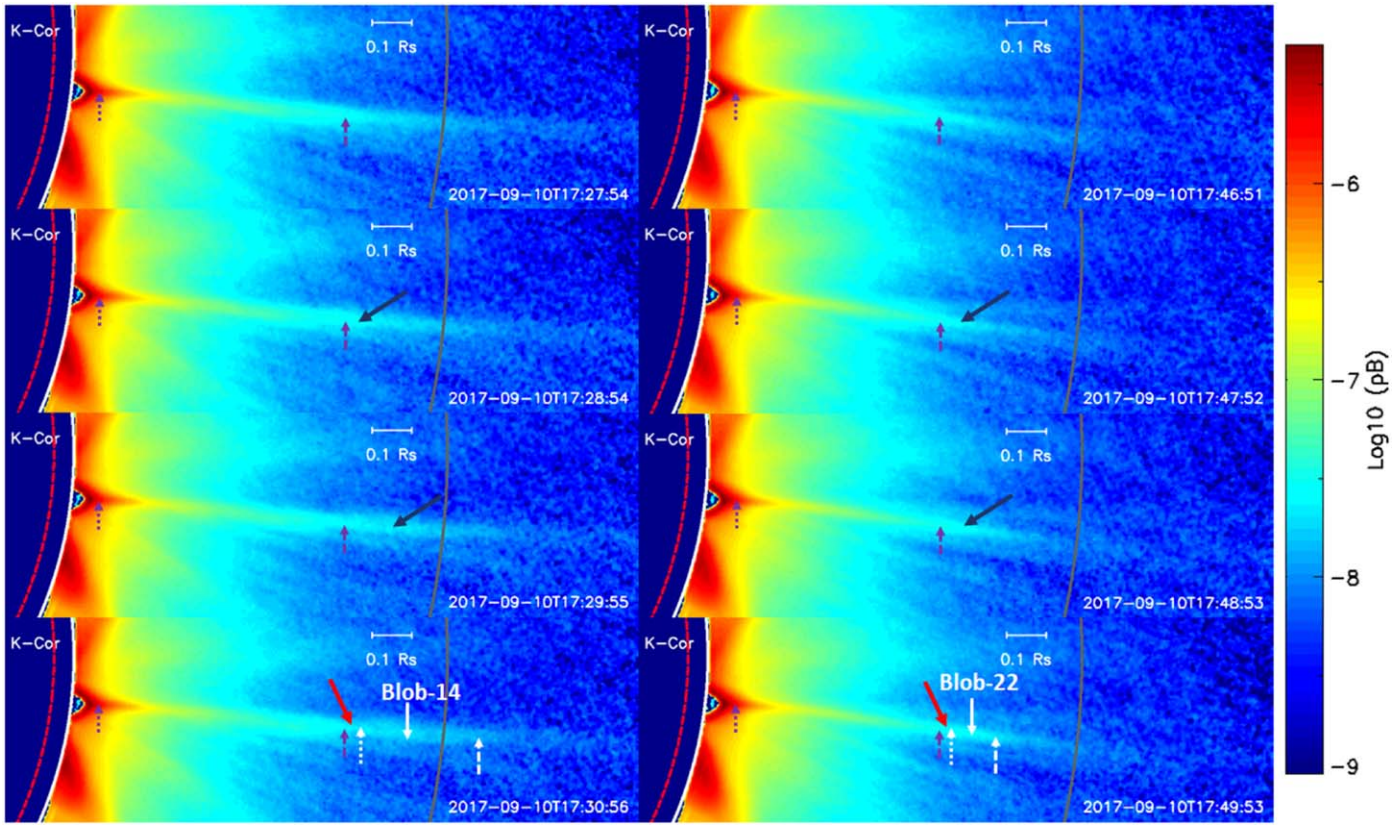

Figure 7. Time sequence of K-Cor intensity images observed on 2017 September 10 from 17:26:53 to 17:30:56 UT (left column) and K-Cor intensity images from 17:46:51 to 17:49:53 UT (right column). "Blob" indicates the K-Cor blobs that appeared above the tips of the post-CME CS. Dark blue and red arrows represent the localized brightness enhancement structures near the tips of the CS and the shrinking regions of the tips of the CS, respectively. The white solid, dashed, and dotted arrows are the same as those in Figure 1. The red dashed, white, gray, and gray dashed partial circles, and purple dashed and dotted arrows are the same as those in Figure 2.

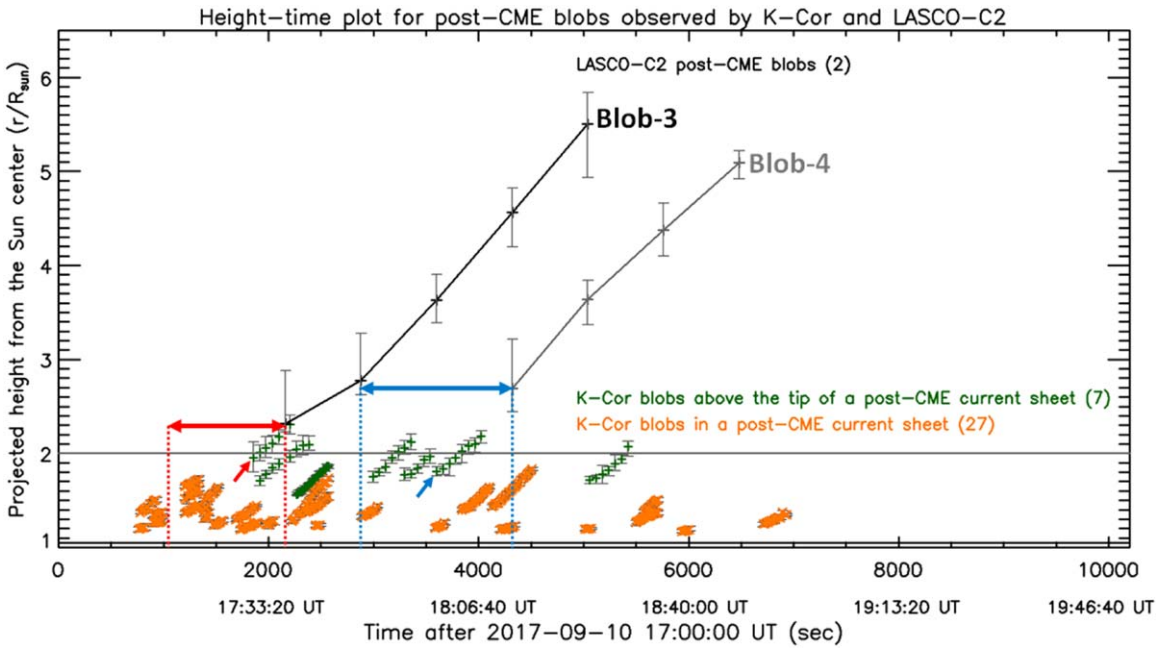

Figure 8. Height–time plot for 34 K-Cor blobs and 2 LASCO-C2 blobs. Black plus symbols with lines represent LASCO-C2 blobs. The two red dotted vertical lines with a double sided horizontal arrow and blue color show the estimated time windows for the detection of inner corona blobs associated with LASCO-C2 "Blob-3" and "Blob-4" respectively. The gray horizontal line corresponds to sizes of the LASCO-C2 occulting disk with a radius of 2.0 $R_{\odot}$. Orange and green symbols, vertical error bars, and the black horizontal line are the same as those in Figure 3.

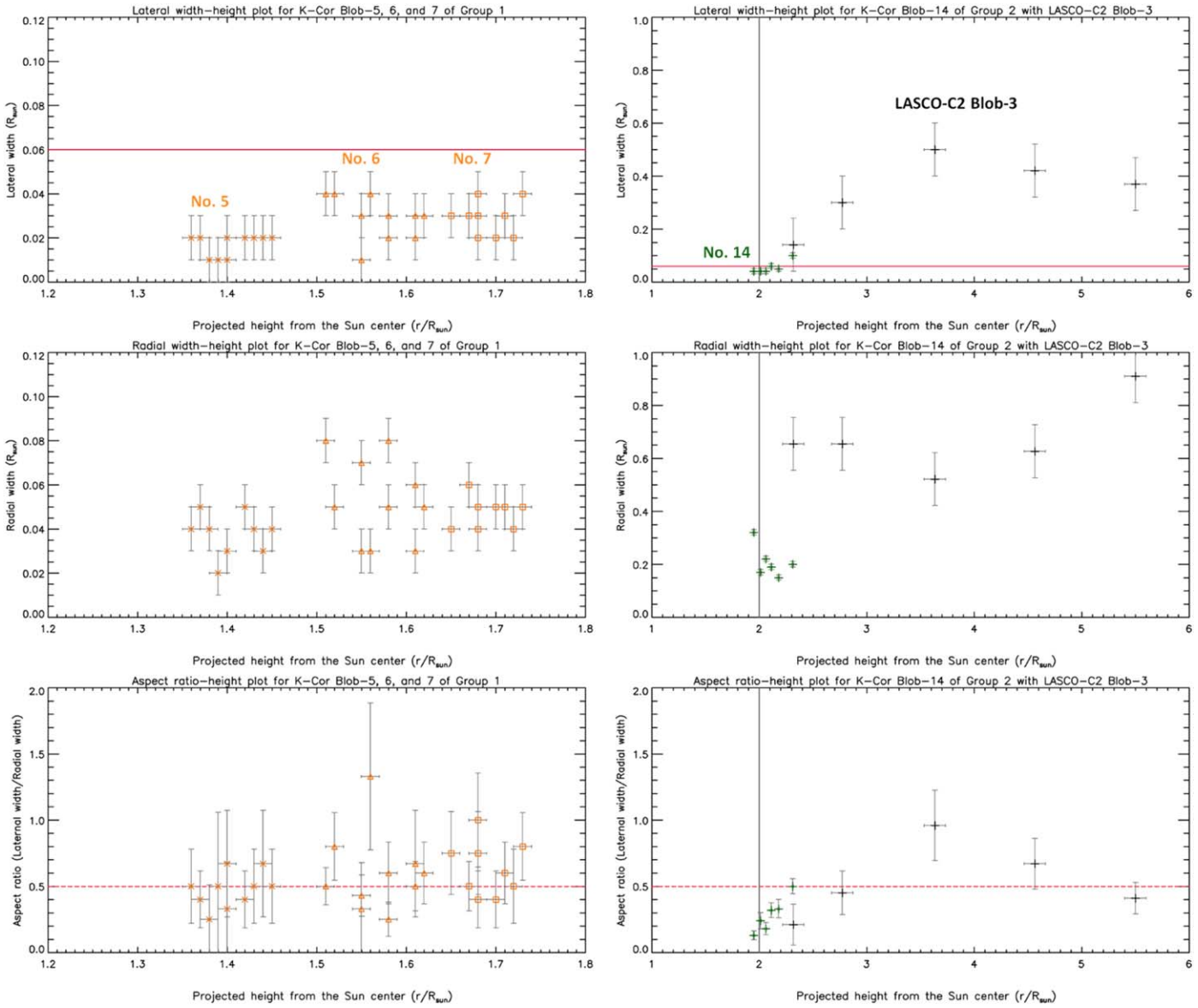

Figure 9. Lateral width, radial width, and aspect ratio-height plots for K-Cor blob 5, 6, and 7 of Group 1 (left column) and for K-Cor blob 14 of Group 2 with LASCO-C2 blob-3 (right column). In the left panel, orange cross, triangle, and square symbols indicate the morphological parameters for K-Cor blobs 5, 6, and 7, respectively. In the right panel, green and black plus symbols indicate the morphological parameters for K-Cor blob 14 and LASCO-C2 blob 3, respectively. The gray vertical line corresponds to sizes of the LASCO-C2 occulting disk with radius of 2.0 $R_{\odot}$. Red solid and dashed lines in the top and bottom panels show the average lateral widths of post-CME CS structures and the average aspect ratio of blobs derived from MHD simulations (Mei et al. 2012), respectively. The gray horizontal error bars indicate the measurement uncertainties caused by the determination of blob locations.

3.5. Morphological Evolutions of Post-CME Blobs

We examine the morphological evolutions of K-Cor blobs shown in the left columns of Figures 6 and 7, which represent the blobs of Groups 1 and 2, respectively. For this, we make the scatter plots between morphological parameters (lateral width, radial width, and aspect ratio) of K-Cor blobs and their appearance heights as shown in Figure 9. We find that Groups 1 and 2 have different morphological evolutions: Group 1 seems to have constant lateral widths, radial widths, and aspect ratios during the propagations although there are variations in each parameter. For example, the average lateral width, radial width, and aspect ratio of K-Cor blob 5 (orange cross symbols) are 0.02 $R_{\odot}$ with standard deviation (SD) of 0.01 $R_{\odot}$, 0.04 $R_{\odot}$ with SD of 0.01 $R_{\odot}$, and 0.47 with SD of 0.13, respectively. Group 2 tends to have lateral width expansion and radial width contraction, which means that the blob becomes more circular during its growth. This is similar to the results from the MHD simulation by Shen et al. (2013) who find that blobs are highly asymmetric soon after being formed, while older blobs tend to be more circular. When we consider outer blobs related to Group 2, Group 2 has lateral and radial width expansions during the propagations. For example, the lateral (radial) width of K-Cor blob 14 and LASCO-C2 blob 3 (green and black plus symbols) change from 0.04 to 0.37 $R_{\odot}$ (from 0.32 to 0.91 $R_{\odot}$) at the heights between 1.95 and 5.5 $R_{\odot}$. Our results show that inner corona blobs formed in the post-CME CS maintain their shapes during their propagations. The other blobs that appeared above the tips of the post-CME CS undergo lateral and radial expansions with expansion rates of 72 and 129 km s^{-1}, respectively.

4. Summary and Discussion

It is expected that LASCO-C2 post-CME blobs form at the heights between 1.0 and 2.0 $R_\odot$, measured from the center of the Sun, and they can be generated by magnetic reconnection triggered by the tearing mode instability in the Sweet–Parker CS (Furth et al. 1963; Shibata & Tanuma 2001; Shen et al. 2011). In this study, we investigate 2 LASCO-C2 blobs and 34 K-Cor blobs as well as their associated post-CME CS structures observed on 2017 September 10 from 17:11 to 18:58 UT to understand the origin and formation mechanism of the LASCO-C2 blobs. By visual inspection of the post-CME CS and its association with blobs in K-Cor and LASCO-C2 images, we find that after a CME eruption, 27 K-Cor blobs are persistently formed in the CS (Group 1) at heights between 1.17 and 1.65 $R_\odot$ and they are generated by the magnetic reconnection process triggered by the tearing mode instability near the middle of the CS, which resembles the Sweet–Parker CS. During the formation and propagation of the K-Cor blobs, seven blobs are consistently occurring near or above the tips of the CS (Group 2) at heights between 1.57 and 1.95 $R_\odot$, and they are generated by tearing mode instability near the tips of the CS, similar to the magnetic reconnection process in the tail of Earth's magnetosphere. Among the seven blobs of Group 2, five blobs cannot be identified in the outer corona (LASCO-C2 FOV) and only two blobs are associated with blobs in the outer corona on their temporal and spatial relationships. Our observations first demonstrate that LASCO-C2 blobs might form at heights from 1.5 to 1.8 $R_\odot$ and they are generated by the tearing mode instability near the tips of post-CME CSs. Our finding about the formation heights of LASCO-C2 blobs is consistent with the idea that the formation heights of LASCO-C2 blobs might be higher than the *SDO*/AIA FOV (Schanche et al. 2016) and similar to the results from Chae et al. (2017) who suggest the formation heights of SECCHI-COR2 post-CME blobs are approximately 1.5 $R_\odot$ by analyzing the kinematics of the seven outward post-CME blobs on 2013 September 21 and 22 by *STEREO*/COR-2B. Our finding about the formation mechanism of LASCO-C2 blobs is similar to the possible formation mechanism for streamer blobs reported by Wang & Sheeley (2000).

By careful investigation of the spacetime plot of K-Cor running difference images along the post-CME CS, we find the candidates of sunward-moving blobs, and their observation heights range from 1.14 to 1.21 $R_\odot$ (Mean = 1.17 $R_\odot$). We also find outward-moving blobs that appear near the heights between 1.20 and 1.43 $R_\odot$ (Mean = 1.26 $R_\odot$). From these results, we can estimate that the magnetic X-points of magnetic reconnection regions might be located near the heights between 1.17 to 1.26 $R_\odot$, which are similar to the result from Cheng et al. (2018) who suggest that the magnetic X-points of magnetic reconnection regions might be located at heights between 1.14 and 1.26 $R_\odot$. Several analytical models and MHD simulations expect that the magnetic X-points steadily move upwards by a CME eruption and its propagation into interplanetary space (Lin & Forbes 2000; Reeves & Forbes 2005; Shen et al. 2011; Mei et al. 2012; Takahashi et al. 2017). If the expectation is right, the formation heights of outward-moving inner corona blobs steadily increase with time. However, as shown in Figure 3, the blob formation heights are near 1.2 $R_\odot$ during the K-Cor observations from 17:12 to 18:39 UT, which are different from the expectation. It might be caused by the change of magnetic X-points being small during the late phase of a CME eruption as shown by the red line of Figure 4 in Forbes et al. (2018).

Regarding to the kinematics of inner corona blobs, we find that Groups 1 and 2 have different kinematics: (1) Group 1 has a broad speed range ($38 \sim 945\,\mathrm{km\,s^{-1}}$) and its speed distribution tends to be dramatically increased with heights ranging from 1.17 to 1.82 $R_\odot$. On the other hand, Group 2 has a narrow speed range ($579 \sim 726\,\mathrm{km\,s^{-1}}$) and its speed distribution tends to be constant with heights from 1.57 to 2.31 $R_\odot$. (2) Group 1 has larger average accelerations (Group 1 $= \langle 4272\,\mathrm{ms^{-2}}\rangle$; Group 2 $= \langle 1418\,\mathrm{ms^{-2}}\rangle$) than those of Group 2. These speed and acceleration profiles are similar to those of CMEs shown in Figure 8 of Bein et al. (2012). From these findings, we estimate that Lorentz forces resulting from magnetic reconnection in a post-CME CS drive a post-CME blob acceleration. We also find that Group 2 has similar kinematics with LASCO-C2 blobs whose speeds range from 767 to $787\,\mathrm{km\,s^{-1}}$ and their speed distributions are similar to those from Song et al. (2012). This might show that a post-CME CS could be one of the origins of a fast solar wind.

By examining the apparent motions of K-Cor blobs, we find that about 68% (23/34) of K-Cor blobs (18 blobs of Group 1 and 5 blobs of Group 2) move steadily faster during their propagations. Our observations are similar to the results using resistivity MHD simulations with the Sweet–Parker CS (Shen et al. 2011; Mei et al. 2012; Forbes et al. 2018), while they are different from the apparent motions of outflow blobs detected by Hinode's XRT observations on 2008 April 9 reported by Savage et al. (2010), who found that XRT blobs propagate with nearly constant speeds (as shown in their Figure 13) and suggest that the motions are caused by the Petschek reconnection process (Petschek 1964). Since many K-Cor blobs undergo an acceleration process, we suggest that the motions of inner corona blobs might be generated by the Sweet–Parker reconnection (Sweet 1958; Parker 1963).

Based on the observations, we propose a schematic model on the formation of the LASCO-C2 blob on 2017 September 10 as shown in Figure 10. The LASCO-C2 blob formations can be explained through the following processes: (1) Initially, inner corona blobs (vertically elongated orange ellipses) are triggered by the tearing mode instability near the middle of the post-CME CS and they propagate outward with increasing speeds along the CS as shown in Figure 10(a). The sunward-moving blob (gray ellipse) also forms above a post-flare arcade. The outward- and sunward-moving motions might be driven by the reconnection outflows generated by the Sweet–Parker magnetic reconnection processes in the CS. Here, red and bright orange explosion symbols show the main magnetic reconnection region including magnetic X-points in the CS and magnetic reconnection region by tearing mode instability near the middle of the CS as described by Furth et al. (1963), respectively. (2) If the outward-moving blobs arrive at the tips of the CS, they are accumulated (dark blue ellipse) while new inner corona blobs and sunward-moving blobs are persistently formed in the CS as shown in Figure 10(b). (3) When the tip of the CS is stretched so extremely, the magnetic reconnection process triggered by the tearing mode instability near the tips of the CS occurs. Newly recognized inner corona blobs (green ellipses) are generated above the tips of the CS and move outward. If the inner corona blobs propagate into the LASCO-C2 FOV, the LASCO-C2 coronagraph can observe these blobs (black ellipses) as shown in Figure 10(c). Here, the purple explosion symbol shows the magnetic reconnection region by tearing

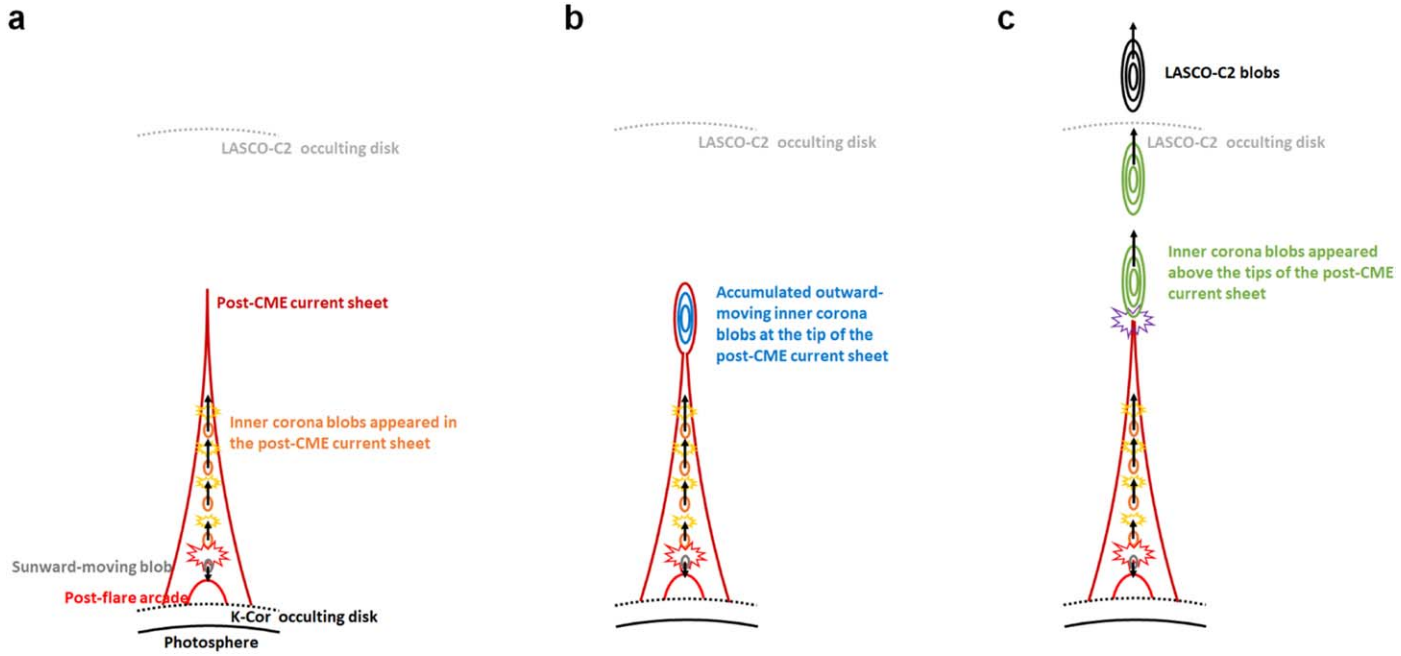

Figure 10. Schematic diagram representing the LASCO-C2 blob formations observed on 2017 September 10 from 17:11 to 18:58 UT. Left panel: initial stage of blob formation indicating the observed locations and appearance motions of inner corona blobs that appeared in the post-CME CS and sunward-moving blobs. Middle panel: middle stage of blob formation showing accumulated outward-moving inner corona blobs at the tip of the CS as well as new inner corona blobs and sunward-moving blobs. Right panel: final stage of blob formation representing the observed locations and appearance motions of inner corona blobs that appeared above the tips of the CS and LASCO-C2 blobs. More detailed descriptions are provided in the text.

mode instability near the tips of the CS as shown in Figure 5 of Sitnov et al. (2002).

Regarding the inner corona observations of a post-CME CS and its associated blobs formed below 2.0 $R_{\odot}$, Ling & Webb et al. (2014) first measure the evolutions of a post-CME CS as well as its associated outward-moving blob structure by using a MK-4 coronameter with spatial resolution ($5\farcs95\,\mathrm{pixel}^{-1}$) and temporal cadence (3 minutes). Recently, Cheng et al. (2018) clearly showed that outward-moving blobs formed near the heights of 1.26 $R_{\odot}$ by using K-Cor having high spatial resolution ($5\farcs5\,\mathrm{pixel}^{-1}$) and temporal cadence (15 s) for the first time. In this study, we show the first clear observational evidence for the formation of outer post-CME blobs above 2.0 $R_{\odot}$ as well as kinematic characteristics of two distinct types of inner post-CME blobs. These results cannot be observed by using MK-4. Therefore, we suggest that high time cadence images are needed to understand the formations of post-CME blobs and CMEs as well as the evolutions of inner corona structures.

We are grateful to the referee and scientific editor for helpful and constructive comments. This research was supported by the Korea Astronomy and Space Science Institute under the R&D program Development of a Solar Coronagraph on International Space Station (Project No. 2020-1-850-07) supervised by the Ministry of Science, ICT and Future Planning. This research was also supported by the Basic Science Research Program through the National Research Foundation of Korea (NRF) funded by the Ministry of Education (2019R1F1A1055071) and the Ministry of Science and ICT (grant No. 2019R1C1C1006033). We thank the *SOHO*/LASCO CME catalog for the LASCO-C2 data and data analysis and K-Cor online database for the K-Cor data. The CME catalog is generated and maintained at the CDAW Data Center by NASA and The Catholic University of America in cooperation with the Naval Research Laboratory. The *SOHO*/LASCO data used here are produced by a consortium of the Naval Research Laboratory (USA), Max-Planck-Institutfür Sonnensystemforschung (Germany), Laboratoire d'Astronomie (France), and the University of Birmingham (UK). *SOHO* is a project of international cooperation between the ESA and NASA. The K-Cor data is courtesy of the Mauna Loa Solar Observatory, operated by the High Altitude Observatory, as part of the National Center for Atmospheric Research (NCAR). N.C. A.R. is supported by the National Science Foundation.

ORCID iDs

Jae-Ok Lee https://orcid.org/0000-0002-7652-7883
Kyung-Suk Cho https://orcid.org/0000-0003-2161-9606
Kyoung-Sun Lee https://orcid.org/0000-0002-4329-9546
Il-Hyun Cho https://orcid.org/0000-0001-7514-8171
Yukinaga Miyashita https://orcid.org/0000-0001-5622-8141
Yeon-Han Kim https://orcid.org/0000-0001-5900-6237
Rok-Soon Kim https://orcid.org/0000-0002-9012-399X
Soojeong Jang https://orcid.org/0000-0001-6854-9823

References

Bein, B. M., Berkebile-Stoiser, S., Veronig, A. M., et al. 2012, ApJ, 738, 191
Brueckner, G. E., Howard, R. A., Koomen, M. J., et al. 1995, SoPh, 162, 357
Chae, J., Cho, K., Kwon, R.-Y., et al. 2017, ApJ, 841, 49
Chandra, B. D. G., & Hollweg, J. V. 2009, ApJ, 707, 1659
Cheng, X., Li, Y., Wan, L. F., et al. 2018, ApJ, 866, 64
Forbes, T. G., Seaton, D. B., & Reeves, K. K. 2018, ApJ, 858, 70
Furth, H. P., Killeen, J., & Rosenbluth, M. N. 1963, PhFl, 6, 459
Gary, D. E., Chen, B., Dennis, B. R., et al. 2018, ApJ, 863, 83
Gopalswamy, N., Yashiro, S., Mäkelä, P., et al. 2018, ApJL, 863, L39
Guo, L.-J., Bhattacharjee, A., & Huang, Y.-M. 2013, ApJL, 771, L14
Howard, R. A., Moses, J. D., Vourlidas, A., et al. 2008, SSRv, 136, 67
Ko, Y.-K., Raymond, J. C., Lin, J., et al. 2003, ApJ, 594, 1068

Kwon, R.-Y., Vourlidas, A., & Webb, D. 2016, ApJ, 826, 94
Lemen, J. R., Title, A. M., Akin, D. J., et al. 2012, SoPh, 275, 17
Lin, J., & Forbes, T. G. 2000, JGR, 105, 2375
Lin, J., Ko, Y.-K., Sui, L., et al. 2005, ApJ, 622, 1251
Lin, J., Li, J., Ko, Y.-K., et al. 2009, ApJ, 693, 1666
Lin, J., Murphy, N. A., Shen, C., et al. 2015, SSRv, 194, 237
Ling, A. G., Webb, D. F., et al. 2014, ApJ, 784, 91
Liu, W., Jin, M., Downs, C., et al. 2018, ApJL, 864, L24
Liu, Y. D., Zhu, B., & Zhao, X. 2019, ApJ, 871, 8
Longcope, D., Unverferth, J., Klein, C., et al. 2018, ApJ, 868, 148
Mei, Z., Shen, C., Wu, N., et al. 2012, MNRAS, 425, 2824
Morgan, H., Habbal, S. R., & Woo, R. 2006, SoPh, 236, 263
Ni, L., & Lukin, V. S. 2018, ApJ, 868, 144
Parker, E. N. 1963, ApJS, 8, 177
Pesnell, W. D., Thompson, B. J., & Chamberlin, P. C. 2012, SoPh, 275, 3
Petschek, H. E. 1964, in AAS-NASA Symposium on the Physics of Solar Flare, ed. W. N. Hess (Washington, DC: NASA), 425
Reeves, K. K., & Forbes, T. G. 2005, ApJ, 610, 1133
Riley, P., Lionello, R., Mikić, Z., et al. 2007, ApJ, 655, 591
Savage, S. L., Mckenzie, D. E., Reeves, K. K., et al. 2010, ApJ, 722, 329
Schanche, N. E., Reeves, K. K., & Webb, D. F. 2016, ApJ, 831, 47
Shen, C., Lin, J., & Murphy, N. A. 2011, ApJ, 737, 14
Shen, C., Lin, J., Murphy, N. A., et al. 2013, PhPl, 20, 072114
Shibata, K., & Tanuma, S. 2001, EP&S, 53, 473
Sitnov, M. I., Sharma, A. S., Guzdar, P. N., et al. 2002, JGRA, 107, 1256
Song, H.-Q., Chen, Y., Li, G., et al. 2012, PhRvX, 2, 021015
Song, H. Q., Kong, X. L., Chen, Y., et al. 2012, SoPh, 276, 261
Sweet, P. A. 1958, in Electromagnetic Phenomena in Cosmical Physics, ed. B. Lehnert (Cambridge: Cambridge Univ. Press), 123
Takahashi, T., Qiu, J., Shibata, K., et al. 2017, ApJ, 848, 102
Vršnak, B., Poletto, G., Vujić, E., et al. 2009, A&A, 499, 905
Wang, Y.-M., Sheeley, J. R., JR., Socker, D. G., et al. 2000, JGRA, 105, 25133
Webb, D. F., Burkepile, J., Forbes, T. G., et al. 2003, JGRA, 108, 1440
Webb, D. F., & Vourlidas, A. 2016, SoPh, 291, 3725